Under consideration for publication in J. Fluid Mech.

Banner appropriate to article type will appear here in typeset article

Helical flows spontaneously generated by salt fingers

Adrian E. Fraser[1], Adrian van Kan[2], Edgar Knobloch[2], Keith Julien[1] and Chang Liu[3]

[1]Department of Applied Mathematics, University of Colorado, Boulder, CO 80309, USA

[2]Department of Physics, University of California at Berkeley, Berkeley, CA 94720, USA

[3]School of Mechanical, Aerospace, and Manufacturing Engineering, University of Connecticut, Storrs, CT 06269, USA

Corresponding author: Adrian E. Fraser, adrian.fraser@colorado.edu

(Received xx; revised xx; accepted xx)

We study the dynamics of salt fingers in the regime of slow salinity diffusion (small inverse Lewis number) and strong stratification (large density ratio), focusing on regimes relevant to Earth's oceans. Using three-dimensional direct numerical simulations in periodic domains, we show that salt fingers exhibit rich, multiscale dynamics in this regime, with vertically elongated fingers that are twisted into helical shapes at large scales by mean flows and disrupted at small scales by isotropic eddies. We use a multiscale asymptotic analysis to motivate a reduced set of partial differential equations that filters internal gravity waves and removes inertia from all parts of the momentum equation except for the Reynolds stress that drives the helical mean flow. When simulated numerically, the reduced equations capture the same dynamics and fluxes as the full equations in the appropriate regime. The reduced equations enforce zero helicity in all fluctuations about the mean flow, implying that the symmetry-breaking helical flow is spontaneously generated by strictly non-helical fluctuations.

1. Introduction

The salt-finger instability occurs in stably stratified fluid layers with background temperature and salinity that both increase with height, and a sufficiently small ratio of salinity diffusivity κ_S to thermal diffusivity κ_T. This instability drives significant turbulent mixing and a broad range of dynamics in the ocean (Radko 2013), where this diffusivity ratio—the inverse Lewis number—is quite small: $\tau \equiv \kappa_S/\kappa_T \approx 10^{-2}$.

In stably stratified systems where heat is the sole contributor to buoyancy, large thermal diffusivity has been leveraged to derive asymptotically reduced sets of PDEs valid in the so-called "low-Péclet number" (LPN) limit (Lignières 1999; Garaud 2021), where the buoyancy equation reduces to a diagnostic balance between advection of the background temperature gradient and diffusion of thermal fluctuations. Given that rapid thermal diffusion is fundamental to the salt-finger instability, one might naturally expect similar asymptotic reductions to be applicable. Indeed, Prat *et al.* (2015) explored the LPN limit for salt fingers in astrophysical regimes (cf. Knobloch & Spruit 1982), where both τ and the ratio of viscous to thermal diffusion, the Prandtl number $Pr \equiv \nu/\kappa_T$, are extremely small (Pr, $\tau \sim 10^{-6}$; Garaud 2018). They found that the LPN limit reproduces the same turbulent fluxes as the full equations in the appropriate limit. The limit of fast thermal diffusion was also studied, albeit in 2D, by Xie *et al.* (2017), who showed, in addition, that in the oceanographic regime of $Pr \gtrsim O(1)$, the momentum equation reduces to a diagnostic balance involving buoyancy and viscosity. In this regime, the evolution is driven by the salinity field alone, with subdominant inertial terms, resulting in inertia-free salt convection (IFSC).

The reductions offered by these limits simplify both numerical and analytical computations while excluding presumably irrelevant dynamics in their respective regimes of validity. For instance, in the LPN limit internal gravity waves are overdamped, and thus a large buoyancy frequency no longer constrains the simulation time step in this limit. However, the regions in parameter space where the excluded dynamics remain important are not always clear *a priori*. The spontaneous formation of thermohaline staircases and the large-scale, secondary instabilities that often precede them (e.g., the collective and gamma instabilities, see Radko 2003; Traxler *et al.* 2011) are excluded in the LPN limit, but these can still occur when τ and/or Pr are extremely small, provided the system is not too strongly stratified (Garaud 2018). Thus, one expects the LPN and IFSC limits to faithfully capture the dynamics of salt fingers provided τ and/or Pr are sufficiently small *and* the density stratification is sufficiently large.

With these uncertainties in mind, we extend here the work of Xie *et al.* (2017) to three dimensions, performing a suite of direct numerical simulations (DNS) of both the primitive and IFSC equations at $\tau = 0.05$ and $Pr = 5$ with varying degrees of stratification, focusing on the limit of strong stratification (weak instability). We find that this regime is characterized by remarkably rich, multiscale dynamics that the IFSC limit fails to recover except in cases with very weak instability. Motivated by the simulation results, we consider a multiscale asymptotic expansion of our system, which points to a natural modification of the IFSC model of Xie *et al.* (2017). This modified IFSC (MIFSC) model reproduces the dynamics seen in simulations of the full equations for much weaker stratification (stronger instability) and suggests how the fields and fluxes might scale with stratification, which we show to be broadly consistent with the simulations.

2. Numerical method

We are interested in the dynamics of salt fingers in the simultaneous limits of fast thermal diffusion and weak or moderate instability. We consider fluctuations atop linear background profiles of salinity and potential temperature in the vertical with constant slopes β_S and β_T, respectively. We assume the flows are slow enough and the layer height small enough to permit the use of the Boussinesq approximation. In this limit, the standard control parameters include the Prandtl number $Pr \equiv \nu/\kappa_T$, the inverse Lewis number $\tau \equiv \kappa_S/\kappa_T$, and the density ratio $R_\rho \equiv \alpha_T\beta_T/(\alpha_S\beta_S)$ with $\alpha_T > 0$, $\alpha_S > 0$ the respective coefficients of expansion. We consider periodic boundary conditions in all directions, in which case our system is linearly unstable to the salt-finger instability for $1 < R_\rho < \tau^{-1}$ (Baines & Gill 1969), with $R_\rho = \tau^{-1}$ corresponding to marginal diffusive stability and $R_\rho < 1$ to an unstably stratified background and hence dynamical instability. In the regime of interest here, it is helpful to introduce the following control parameters:

$$Ra = \frac{\alpha_S\beta_S\kappa_T}{\alpha_T\beta_T\kappa_S} = \frac{1}{R_\rho\tau}, \quad \mathcal{R} \equiv Ra - 1 \quad \text{and} \quad Sc \equiv \frac{\nu}{\kappa_S} = \frac{Pr}{\tau}, \tag{2.1}$$

where Ra is the Rayleigh ratio (with marginal stability now at $Ra = 1$), $\mathcal{R}$ is a measure of supercriticality and Sc is the Schmidt number. In all results presented below, we fix $Pr = 5$, $\tau = 0.05$ and thus $Sc = 100$.

We follow Sec. 3.1 of Xie *et al.* (2017) in our choice of nondimensionalization, taking the characteristic finger width $d = (\kappa_T \nu / g \alpha_T \beta_T)^{1/4}$ (with gravitational acceleration g) as the length scale and the salinity diffusion time d^2/κ_S as the timescale. As our temperature scale, we take the background temperature difference across a height d rescaled by τ, yielding $\tau \beta_T d$. Similarly, our unit for salinity fluctuations is the background salinity difference across d rescaled by Ra^{-1}, yielding $Ra^{-1}\beta_S d$. The governing equations are

$$\frac{1}{Sc}\left(\frac{\partial}{\partial t} + \mathbf{u}\cdot\nabla\right)\mathbf{u} = -\nabla p + (T - S)\hat{\mathbf{z}} + \nabla^2 \mathbf{u}, \tag{2.2}$$

$$\nabla \cdot \mathbf{u} = 0, \tag{2.3}$$

$$\tau\left(\frac{\partial}{\partial t} + \mathbf{u}\cdot\nabla\right)T + w = \nabla^2 T, \tag{2.4}$$

and

$$\left(\frac{\partial}{\partial t} + \mathbf{u}\cdot\nabla\right)S + Ra\, w = \nabla^2 S, \tag{2.5}$$

with velocity $\mathbf{u} = (u, v, w)$ and temperature, salinity, and pressure fluctuations T, S and p.

In what follows, we present DNS of the above system for different values of Ra. These simulations were performed using the pseudospectral-tau method implemented in Dedalus v2 (Burns *et al.* 2020). We use periodic boundary conditions with a horizontal domain size of $(L_x, L_y) = (4 \times 2\pi/k_{\rm opt}, 2 \times 2\pi/k_{\rm opt})$, where $k_{\rm opt}(Pr, \tau, R_\rho)$ is the horizontal wavenumber at which the linear instability is most unstable for a given set of parameters (for a subset of our parameters, we have checked that the dynamics and time-averaged fluxes change negligibly upon increasing L_x and L_y). For the parameters of interest, the salt fingers become very extended in z, and thus our domain height must be very large to avoid artificial domain-size effects (see, e.g., Appendix A.3 of Traxler *et al.* 2011). For most of the cases reported here, we find $L_z = 64 \times 2\pi/k_{\rm opt}$ to be sufficient (where we confirm this by comparing against results with $L_z = 128 \times 2\pi/k_{\rm opt}$), although we find that shorter domains suffice for $\mathcal{R} \gtrsim 1$, while taller domains are necessary for $\mathcal{R} \lesssim 1/8$. We dealias using the standard 3/2-rule and use a numerical resolution of 8 Fourier modes per $2\pi/k_{\rm opt}$ in each direction, although twice this resolution becomes necessary (as verified by convergence checks) for our simulations with the largest values of $\mathcal{R}$. Note that, per our dealiasing procedure, nonlinearities are evaluated on a grid with $3/2$ times this resolution. We timestep using a semi-implicit, second-order Adams-Bashforth/backwards difference scheme (Dedalus' "SBDF2" option, Eq. [2.8] of Wang & Ruuth 2008), with nonlinearities treated explicitly and all other terms treated implicitly, and an advective CFL safety factor of 0.3 (sometimes 0.15 for our highest $\mathcal{R}$ cases). We initialize simulations with small-amplitude noise in S.

3. Trends across $\mathcal{R}$

Figure 1 shows velocity snapshots from simulations with $\mathcal{R} = 1/80$ (panels a-c), $1/10$ (panels d-f) and 1 (panels g-i), i.e., $R_\rho \simeq 19.75$, 18.18 and 10, illustrating general trends in this regime. In each case, we see highly anisotropic and multiscale dynamics, with vertically elongated, large-amplitude structures (the characteristic salt fingers) in w, and

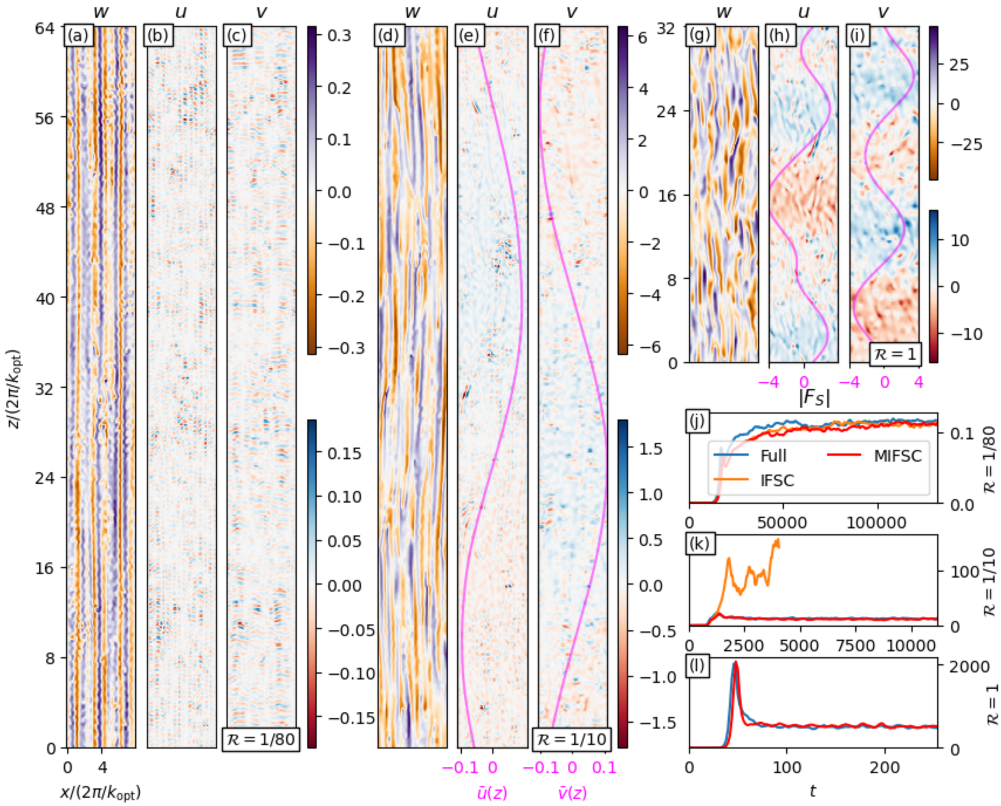

Figure 1. Flow velocity snapshots at $y = 0$ in the saturated state from simulations of equations (2.2)-(2.5) with varying supercriticality: $\mathcal{R} = 1/80$ (a-c), $\mathcal{R} = 1/10$ (d-f) and $\mathcal{R} = 1$ (g-i), with timetraces of the corresponding salinity flux shown in panels j, k, and l, respectively, alongside fluxes from different reduced models (see Sec. 4). All cases exhibit a multiscale and anisotropic flow where fingers with large vertical extent and vertical velocity (compared to horizontal width and velocity) coexist with small-scale, isotropic disturbances. Magenta curves (panels e, f, h, and i) show the time-average (over the saturated state) of the horizontal, helical mean flow $\bar{\mathbf{u}}_\perp$ that becomes a significant feature for $\mathcal{R} \gtrsim 0.1$.

smaller-amplitude, isotropic eddies seen in each velocity field. The separation between the long vertical and the short isotropic scales shrinks as $\mathcal{R}$ increases.

At very small $\mathcal{R}$ (see panels a-c), the fingers become vertically invariant "elevator modes"[1] disturbed by isotropic ripples. For moderate supercriticality, $\mathcal{R} \sim 0.1$, the fingers are no longer vertically invariant but still very anisotropic, with much larger vertical scale and velocity than in the horizontal.

In this regime, a horizontal mean flow $\bar{\mathbf{u}}_\perp$ (where an overbar denotes horizontal averaging) develops spontaneously (cf. Liu *et al.* 2024), as shown by the magenta curves in panels e-f. The two components of $\bar{\mathbf{u}}_\perp$ are $\pi/2$ out of phase in z—i.e., one component passes through 0 as the other reaches an extremum—resulting in a strongly helical mean flow that advects the fingers into a corkscrew-like shape. In fact, this

[1]At larger $\mathcal{R}$, self-connecting structures only persist for insufficiently tall domains and lead to bursty and domain height-dependent dynamics. At very small $\mathcal{R}$, self-connecting structures persist in even the tallest domains we can reasonably achieve numerically, but they do not drive bursty dynamics or domain height-dependent dynamics.

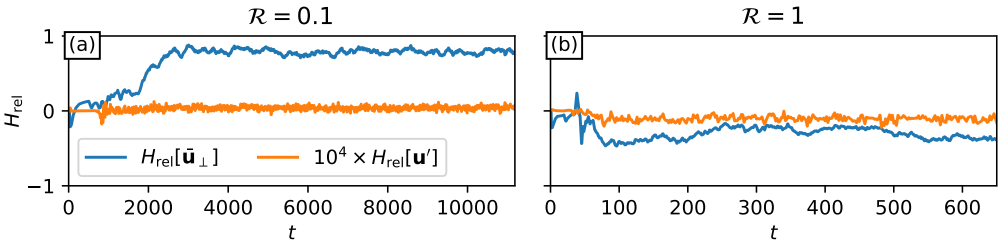

Figure 2. Relative helicity (see text) of the mean flow (blue) and of the fluctuations about the mean flow (orange; multiplied by 10^4 to ease comparison) for two values of $\mathcal{R}$. At small $\mathcal{R}$, the flow is almost maximally helical, and in both cases the fluctuations are highly non-helical, with $H_{\mathrm{rel}}[\mathbf{u}'] \sim 10^{-5}$.

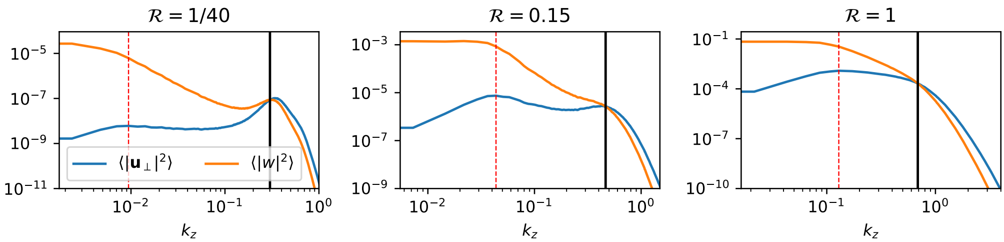

Figure 3. Horizontal (blue) and vertical (orange) kinetic energy spectra versus k_z at $k_y = 0$ and $k_x = k_{\mathrm{opt}}$. Black lines show $k_z = k_{\mathrm{opt}}$ to highlight the small-scale isotropic flow component while the red vertical lines correspond to the secondary peak in the horizontal spectrum to highlight the anisotropic, small k_z flow component. The ratio between these two wavenumbers provides one measure of anisotropy shown in Fig. 4.

mean flow is nearly a *maximally helical* (Beltrami) flow in that its relative helicity $H_{\mathrm{rel}}[\mathbf{u}] \equiv \int \mathbf{u} \cdot (\nabla \times \mathbf{u})\, \mathrm{d}V / [(\int |\mathbf{u}|^2\, \mathrm{d}V)(\int |\nabla \times \mathbf{u}|^2 \mathrm{d}V)]^{1/2}$, calculated using the time- and horizontally-averaged flow, is over 0.99—alternatively, H_{rel} of the instantaneous mean flow saturates at roughly 0.8, see Fig. 2. While $H_{\mathrm{rel}} > 0$ for this particular simulation, other random initial conditions lead to $H_{\mathrm{rel}} < 0$ (not shown) with no clear statistical preference between the two signs based on our limited sample. In stark contrast to the strongly helical mean flow, the relative helicity of the fluctuations about the mean is roughly 10^{-5}. This leads to the remarkable observation that the system spontaneously forms a symmetry-breaking, maximally helical flow from nonhelical fluctuations, similar to that observed by Słomka & Dunkel (2017), Agoua *et al.* (2021) and Romeo *et al.* (2024).

For yet larger $\mathcal{R}$ (see Fig. 1 panels g-i), both the mean flow and the fingers become more vigorous, and the anisotropy of the fingers is less extreme, permitting shorter vertical domains. In this regime, the mean flow is still very helical at each z, but tends to have a shorter length scale and its helicity may change sign with z (see Fig. 2 panel b).

Both the multiscale aspect of this system and the trends in scale separation with $\mathcal{R}$ are readily seen in Fig. 3, which shows spectra of the kinetic energy as a function of the vertical wavenumber k_z at $k_\perp = k_{\mathrm{opt}}$, the fastest-growing wavenumber of the linear instability. Two distinguishing features are seen most clearly in the horizontal kinetic energy, which has a local maximum (or otherwise a clear change in the spectrum, in the case of large $\mathcal{R}$) at isotropic scales where $k_z \sim k_{\mathrm{opt}}$, indicated by the black vertical lines, and a local maximum at smaller k_z indicated by the red vertical lines. Note that the gap in k_z between these two local maxima shrinks as $\mathcal{R}$ increases, consistent with the observed decrease in scale separation with increasing $\mathcal{R}$ (Fig. 1).

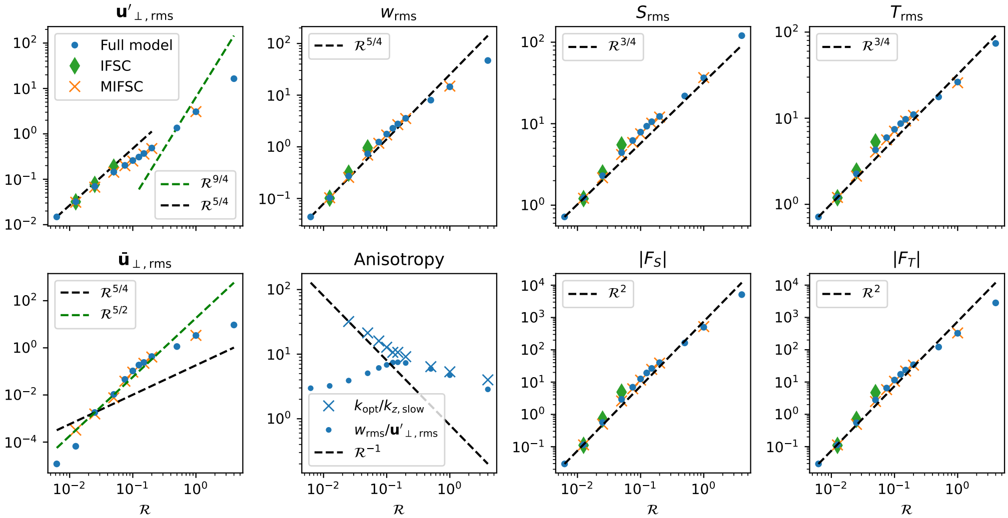

Figure 4. Scalings with respect to $\mathcal{R}$ of several quantities (indicated in the caption for each panel) for the full system, Eqs. (2.2)-(2.5) (blue dots), the IFSC model, with Eqs. (2.4) and (2.2) replaced by Eqs. (4.1) and (4.2) (green diamonds), and the modified IFSC (MIFSC) model, where Eq. (2.2) is replaced instead by Eqs. (4.14)-(4.15) (orange crosses). Black dashed lines show scalings predicted by the multiscale asymptotic analysis described in the text. The green dashed lines and the two measures of anisotropy are described in the text.

4. Asymptotic models

The IFSC model of Xie *et al.* (2017), in three dimensions (3D), is appropriate when $\tau \ll 1$ and $Sc \gg 1$ and is described by the equations

$$w = \nabla^2 T, \tag{4.1}$$

$$0 = -\nabla p + (T - S)\hat{\mathbf{z}} + \nabla^2 \mathbf{u}, \tag{4.2}$$

with Eqs. (2.3) and (2.5) left unchanged. While it appears that the model should be valid for all order one $\mathcal{R}$, we show in Fig. 1 that this is not the case: the model does produce dynamics and fluxes consistent with the full system at sufficiently small supercriticality, roughly $\mathcal{R} \lesssim 1/80$, but for $\mathcal{R} \approx 1/20$ or larger, it produces dynamics that differ qualitatively from solutions of the full equations—while the full system exhibits helical mean flows that disrupt and twist the fingers on large scales, the IFSC model removes the Reynolds stress term from the horizontal mean of Eq. (2.2) and thus lacks these flows. Without mean flows to disrupt the long fingers, such fingers drive temporally bursty dynamics that dramatically raise the fluxes, as shown by the IFSC curve in panel k of Fig. 1.

However, the IFSC model can be modified to capture mean flow generation. Our simulations suggest that anisotropy is an essential aspect of a reduced description of salt fingers valid in the regime depicted in Fig. 1, possibly with a rescaling of the various fields to retain the Reynolds stress at leading order. In order to capture both the elongated fingers shown in Fig. 1 and the small scale isotropic fluctuations therein, we employ a multiscale asymptotic analysis inspired by a related approach to turbulence in stably stratified fluids employed by Chini *et al.* (2022),Shah *et al.* (2024), and Garaud *et al.* (2024).

To begin, we note that the growth rate and optimal wavenumber of the linear instability scale as $\mathcal{R}^{3/2}$ and $\mathcal{R}^{1/4}$, respectively, for sufficiently small $\mathcal{R}$—for the Pr, τ considered here, this scaling is achieved for $\mathcal{R} \lesssim 1$ (see, e.g., Fig. 3 of Xie *et al.* 2017). It is thus convenient to rescale the independent and dependent variables as follows (cf. Radko 2010):

$$\mathbf{x} \mapsto \mathcal{R}^{-1/4}\mathbf{x}, \quad t \mapsto \mathcal{R}^{-3/2}t, \quad \mathbf{u} \mapsto \mathcal{R}^{5/4}\mathbf{u}, \quad p \mapsto \mathcal{R}^{3/2}p, \quad (T,S) \mapsto \mathcal{R}^{3/4}(T,S). \tag{4.3}$$

Equations (2.2)-(2.5) then become

$$\mathcal{R}\frac{1}{Sc}\left(\frac{\partial}{\partial t} + \mathbf{u}\cdot\nabla\right)\mathbf{u} = -\nabla p + \mathcal{R}^{-1}(T-S)\hat{\mathbf{z}} + \nabla^2\mathbf{u}, \tag{4.4}$$

$$\mathcal{R}\tau\left(\frac{\partial}{\partial t} + \mathbf{u}\cdot\nabla\right)T + w = \nabla^2 T, \tag{4.5}$$

and

$$\mathcal{R}\left(\frac{\partial}{\partial t} + \mathbf{u}\cdot\nabla\right)S + Ra\, w = \nabla^2 S, \tag{4.6}$$

with Eq. (2.3) left unchanged. When $\mathcal{R} = O(1)$ but $\tau \ll 1$ and $Sc \gg 1$, the inertial terms in Eqs. (4.4)-(4.5) drop out and the resulting equations correspond to the 3D IFSC model with Eq. (4.6) providing the sole prognostic equation. On the other hand, when $\mathcal{R} \ll 1$, we may expand all fields as asymptotic series in $\mathcal{R}$ as $q = \sum_n q_n\mathcal{R}^n$. Inspecting the z component of Eq. (4.4) in the limit $\mathcal{R} \to 0$ shows that $T_0 = S_0$, i.e., the dynamics are neutrally buoyant (or asymptotically spicy) in this limit. In the following it is helpful to introduce the buoyancy $b \equiv \mathcal{R}^{-1}(T-S)$ and subtract Eq. (4.5) from Eq. (4.6), yielding

$$\left(\frac{\partial}{\partial t} + \mathbf{u}\cdot\nabla\right)(S - \tau T) + w = -\nabla^2 b. \tag{4.7}$$

Next, inspired by the work of Chini *et al.* (2022) and Shah *et al.* (2024), we introduce appropriate fast and slow vertical scales but consider a single horizontal scale only. We further take the fast vertical scale to be isotropic, so that the slow vertical scale captures the elongated fingers seen in Fig. 1. For this purpose, we take $\partial_z \mapsto \alpha^{-1}\partial_{z_s} + \partial_{z_f}$ with $\alpha \gg 1$, and let $q = \langle q\rangle_f + \tilde{q}$, where $\langle\cdot\rangle_f$ represents an average over z_f. Furthermore, noting that the mean flow develops on a slow timescale relative to the growth and saturation of the primary instability (compare Fig. 2 to panels k and l of Fig. 1), we assume that $\langle\bar{\mathbf{u}}_\perp\rangle_f$ varies on a slow timescale, so that $\partial_t\langle\bar{\mathbf{u}}_\perp\rangle_f \mapsto \alpha^{-1}\partial_{t_s}$. Rescaling $\left\langle\mathbf{u}'_\perp\right\rangle_f \mapsto \alpha^{-1}\left\langle\mathbf{u}'_\perp\right\rangle_f$ and $\langle p\rangle_f \mapsto \alpha^{-1}\langle p\rangle_f$ (where primed quantities denote fluctuations about the mean: $q' \equiv q - \bar{q}$), the resulting equations reduce at leading order in $\mathcal{R} \ll 1$ and $\tau \ll 1$ to:

$$\langle w\rangle_f = \nabla_\perp^2\langle T\rangle_f \quad \text{and} \quad \tilde{w} = \nabla_f^2\tilde{T}, \tag{4.8}$$

$$\left[\frac{\partial}{\partial t} + \langle\bar{\mathbf{u}}_\perp\rangle_f\cdot\nabla_\perp\right]\langle S\rangle_f + \left\langle\tilde{\mathbf{u}}\cdot\nabla_f\tilde{S}\right\rangle_f + \langle w\rangle_f = -\nabla_\perp^2\langle b\rangle_f, \tag{4.9}$$

$$\left[\frac{\partial}{\partial t} + \langle\bar{\mathbf{u}}_\perp\rangle_f\cdot\nabla_\perp + \langle w\rangle_f\frac{\partial}{\partial z_f}\right]\tilde{S} + \tilde{\mathbf{u}}\cdot\nabla_f\tilde{S} - \left\langle\tilde{\mathbf{u}}\cdot\nabla_f\tilde{S}\right\rangle_f + \tilde{\mathbf{u}}_\perp\cdot\nabla_\perp\langle S\rangle_f + \tilde{w} = -\nabla_f^2\tilde{b}, \tag{4.10}$$

$$0 = -\nabla_\perp\langle p\rangle_f + \langle b\rangle_f\hat{\mathbf{z}} + \nabla_\perp^2\langle\mathbf{u}'\rangle_f \quad \text{and} \quad 0 = -\nabla_f\tilde{p} + \tilde{b}\hat{\mathbf{z}} + \nabla_f^2\tilde{\mathbf{u}}', \tag{4.11}$$

$$\frac{\partial}{\partial t_s}\langle\bar{\mathbf{u}}_\perp\rangle_f + \frac{\partial}{\partial z_s}\left\langle\overline{\tilde{\mathbf{u}}_\perp\tilde{w}}\right\rangle_f = \frac{Sc}{\mathcal{R}}\frac{1}{\alpha}\frac{\partial^2}{\partial z_s^2}\langle\bar{\mathbf{u}}_\perp\rangle_f, \tag{4.12}$$

$$\nabla_s \cdot \langle \mathbf{u}' \rangle_f = 0 \quad \text{and} \quad \nabla_f \cdot \tilde{\mathbf{u}}' = 0, \tag{4.13}$$

where we have introduced $\nabla_s \equiv (\partial_x, \partial_y, \partial_{z_s})$ and $\nabla_f \equiv (\partial_x, \partial_y, \partial_{z_f})$. Taking $\alpha = Sc/\mathcal{R} \gg 1$ results in a balance between Reynolds stress and viscous dissipation in Eq. (4.12). The structure of this system of equations is broadly similar to the IFSC model: the temperature equations reduce to a diagnostic balance between diffusion and advection of the background, the salinity equations retain nonlinearity on fast scales (and so do not yield a quasilinear structure as in the work of Chini *et al.* 2022), and the momentum equations for fluctuations about the mean flow involve a dominant balance between pressure, buoyancy, and viscosity. However, in contrast to the IFSC model, Eq. (4.12) retains the Reynolds stress term absent from Eq. (4.2). Thus, modifying the IFSC model to capture the leading-order dynamics of the full equations in this limit merely requires retaining the Reynolds stress in the $\mathbf{k}_\perp = 0$ component of the momentum equation:

$$\frac{1}{Sc}\left(\frac{\partial}{\partial t}\bar{\mathbf{u}}_\perp + \frac{\partial}{\partial z}\overline{\mathbf{u}'_\perp w'}\right) = \frac{\partial^2}{\partial z^2}\bar{\mathbf{u}}_\perp, \tag{4.14}$$

$$0 = -\nabla p' + (T' - S')\hat{\mathbf{z}} + \nabla^2 \mathbf{u}', \tag{4.15}$$

with temperature given by Eq. (4.1), and Eqs. (2.3) and (2.5) retained in full. Figure 1 shows that this modified IFSC (MIFSC) model captures the same dynamics as the full equations even for $\mathcal{R} = O(1)$.

The rescaling applied to arrive at the above multiscale asymptotic system offers a natural suggestion for the scaling of the various fields in this limit. For Eqs. (2.2)-(2.5), this analysis predicts that both S and T should scale as $\mathcal{R}^{3/4}$, $\bar{\mathbf{u}}_\perp$ and w as $\mathcal{R}^{5/4}$, and the scaling of $\mathbf{u}'_\perp$ should differ between fast and slow scales in z, with $\left\langle \mathbf{u}'_\perp \right\rangle_f \sim \mathcal{R}^{9/4}$ and $\tilde{\mathbf{u}}'_\perp \sim \mathcal{R}^{5/4}$. The predicted stronger $\mathcal{R}$ dependence of $\left\langle \mathbf{u}'_\perp \right\rangle_f$ is consistent with Fig. 3, which shows that the horizontal kinetic energy peaks at large k_z for small $\mathcal{R}$ but at small k_z for large $\mathcal{R}$.

We present a more quantitative comparison between these predictions and DNS in Fig. 4 by calculating the root-mean-square (r.m.s.) of $\mathbf{u}'_\perp$, $\bar{\mathbf{u}}_\perp$, w, S and T, and the volume-averaged fluxes $F_S = \langle wS \rangle$ and $F_T = \langle wT \rangle$, with the blue dots corresponding to DNS of the full equations, green diamonds to the IFSC model, and orange crosses to the modified IFSC model. Anisotropy is quantified by two means: using the wavenumber ratio corresponding to the two spectral peaks in Fig. 3 (plus symbols; the lowest $\mathcal{R}$ values are suppressed because the low k_z peak is difficult to identify and is likely constrained by domain size), and the ratio $w_{\mathrm{rms}}/\mathbf{u}'_{\perp,\mathrm{rms}}$ (dots). In each panel, black dashed lines correspond to the predicted scalings (for $\mathbf{u}'_{\perp,\mathrm{rms}}$, the black line shows the predicted $\tilde{\mathbf{u}}'_\perp \sim \mathcal{R}^{5/4}$ scaling while the green line shows the $\left\langle \mathbf{u}'_\perp \right\rangle_f \sim \mathcal{R}^{9/4}$ scaling). The scalings of most of these quantities are consistent with predictions as $\mathcal{R} \to 0$, especially w_{rms}, S_{rms}, T_{rms}, F_S and F_T, with the anisotropy measurement inconclusive. In contrast, the r.m.s. of the mean flow, $\bar{\mathbf{u}}_{\perp,\mathrm{rms}}$, follows the predicted $\mathcal{R}^{5/4}$ scaling at larger $\mathcal{R}$ only.[2]

5. Conclusions

We have explored the dynamics of salt fingers in 3D and in the limit of slow salinity diffusion ($\tau \ll 1$, $Pr/\tau \gg 1$) and weak or moderate instability ($\mathcal{R} \equiv R_\rho^{-1}\tau^{-1} - 1 \leq 4$). This regime was studied in 2D by Xie *et al.* (2017), who showed that the temperature

[2]It is worth noting, however, that the mean flow is very weak and evolves very slowly at the smallest values of $\mathcal{R}$, and is thus difficult to measure precisely.

equation reduces to a diagnostic balance akin to the low-Péclet number limit of Lignières (1999) (see also Prat *et al.* 2015; Garaud 2021) and that the vorticity equation is governed by a diagnostic balance between buoyancy and viscous diffusion; Xie et al. referred to these reduced equations as the inertia-free salt convection (IFSC) model.

Simulations of the full equations in 3D exhibit significant departures from the 2D system. First, the 3D case is characterized by rich, multiscale dynamics where anisotropic fingers are twisted at large scales by a helical mean flow and disrupted at small scales by isotropic eddies. This helical mean flow is a maximally helical, Beltrami flow in some regimes, with helicity of either sign depending on the random initial conditions, and provides a striking example of spontaneous symmetry breaking, much as occurs in the systems studied by Słomka & Dunkel (2017), Agoua *et al.* (2021) and Romeo *et al.* (2024). Second, 3D simulations of the IFSC model exhibit qualitatively different dynamics and significantly enhanced fluxes over the full equations unless the instability is very weak ($\mathcal{R} \ll 0.1$)—a consequence of the exclusion of Reynolds stresses in the IFSC model.

The observed multiscale dynamics inform a multiscale asymptotic expansion in the supercriticality $\mathcal{R}$ where the leading-order equations form a closed system. This analysis identifies the leading-order terms missing from the IFSC model—the Reynolds stresses in the equations for the horizontal mean flow—and predicts the scaling of the various fields and fluxes with $\mathcal{R}$. Simulations of the full equations are consistent with these predictions except for the scaling of the mean flow, which has a stronger dependence on $\mathcal{R}$ than suggested by the asymptotic analysis. Furthermore, simulations of the MIFSC equations—the IFSC equations with Reynolds stresses retained—yield qualitative and quantitative agreement with DNS of the full equations up to $\mathcal{R} \approx 1$, further supporting the derived leading-order balances.

A noteworthy feature of the MIFSC model is that, to leading order, the fluctuations $\mathbf{u}'_\perp \equiv \mathbf{u}_\perp - \bar{\mathbf{u}}_\perp$ have strictly zero helicity. Thus, the helical flow represents a spontaneous symmetry-breaking instability arising from *asymptotically non-helical* fluctuations, analogous to the development of unidirectional traveling waves in reflection-symmetric systems (Knobloch *et al.* 1986).

Our computations of the r.m.s. values of the various fields broadly support the scalings with $\mathcal{R}$ predicted from the asymptotic analysis. For comparison, Garaud *et al.* (2024) devised a means to extract the scalings of fast-averaged quantities $\langle q \rangle_f$ and their fluctuations $\tilde{q}$ separately, demonstrating that their scalings differed in their system. In the present case, our asymptotic analysis points to fields other than $\mathbf{u}'_\perp$ exhibiting identical scalings on fast and slow scales. While we find no clear discrepancies in our simulations, future work should extend the approach of Garaud *et al.* (2024) to the present system to test these predictions more carefully.

Our reduced equations—and those of Xie *et al.* (2017) and Prat *et al.* (2015)—indicate that for $\tau \ll 1$ the dynamics no longer depend on Pr and τ separately, and only depend on the combination $Sc \equiv Pr/\tau$. Thus, while we have only simulated the full equations at $Pr = 5$, we may expect our simulations of the reduced equations at $Sc = 100$ to be consistent with the full system in the astrophysically relevant regime of small $Pr, \tau \sim 10^{-7}$-10^{-4} (Prat *et al.* 2015; Skoutnev & Beloborodov 2024). We are thus led to expect that helical flows may form in the interiors of stars, an exciting prospect due to their tendency to support dynamo growth (Rincon 2019; Tobias 2021).

Both the reduced and the full equations admit (unstable) single-mode solutions that may provide a useful proxy for flux computations in the strongly nonlinear regime, and investigations of the role played by the helical mean flow. Outstanding questions involve possible reversals of this flow in longer simulations, and the generation of such flows in vertically confined domains. The multiparameter nature of the problem raises additional questions involving distinct asymptotic regimes when both τ and Sc^{-1} are small and if $Sc = O(1)$ in the regime of small τ and Pr—note that $Sc \sim 10^2$ is likely in stars.

Acknowledgements K.J. passed away before this manuscript was finalised. We have attempted to present the results of our collaboration in accordance with his high standards. Any errors or misinterpretations remain our own. A.F. thanks Ian Grooms and Brad Hindman for many useful discussions about helicity and multiscale asymptotic analyses.

Funding This work was supported by NSF under grants OCE-1912332 (A.F. and K.J.), AST-2402142 (A.F.) and DMS-2308337 (A.v.K. and E.K.). The computational resources were provided by the NSF ACCESS program (projects PHY250118 and PHY230056), allowing us to utilize the Purdue Anvil CPU cluster.

Declaration of interests The authors report no conflict of interest.

References

Agoua, W., Favier, B., Delache, A., Briard, A. & Bos, W.J.T. 2021 Spontaneous generation and reversal of helicity in anisotropic turbulence. *Phys. Rev. E* **103**, L061101.

Baines, P.G. & Gill, A.E. 1969 On thermohaline convection with linear gradients. *J. Fluid Mech.* **37**, 289–306.

Burns, K.J., Vasil, G.M., Oishi, J.S., Lecoanet, D. & Brown, B.P. 2020 Dedalus: A flexible framework for numerical simulations with spectral methods. *Phys. Rev. Res.* **2**, 023068.

Chini, G.P., Michel, G., Julien, K., Rocha, C.B. & Caulfield, C.P. 2022 Exploiting self-organized criticality in strongly stratified turbulence. *J. Fluid Mech.* **933**, A22.

Garaud, P. 2018 Double-diffusive convection at low Prandtl number. *Ann. Rev. Fluid Mech.* **50**, 275–298.

Garaud, P. 2021 Journey to the center of stars: The realm of low Prandtl number fluid dynamics. *Phys. Rev. Fluids* **6**, 030501.

Garaud, P., Chini, G.P., Cope, L., Shah, K. & Caulfield, C.P. 2024 Numerical validation of scaling laws for stratified turbulence. *J.Fluid Mech.* **991**, R1.

Knobloch, E., Deane, A.E., Toomre, J. & Moore, D.R. 1986 Doubly diffusive waves. *Contemp. Math* **56**, 203–216.

Knobloch, E. & Spruit, H.C. 1982 Stability of differential rotation in stars. *Astron. Astrophys.* **113**, 261–268.

Lignières, F. 1999 The small-Péclet-number approximation in stellar radiative zones. *Astron. Astrophys.* **348**, 933–939.

Liu, C., Sharma, M., Julien, K. & Knobloch, E. 2024 Fixed-flux Rayleigh–Bénard convection in doubly periodic domains: generation of large-scale shear. *J. Fluid Mech.* **979**, A19.

Prat, V., Lignières, F. & Lagarde, N. 2015 Numerical simulations of zero-Prandtl-number thermohaline convection. In *SF2A-2015: Proc. Annu. Meet. French Soc. Astron. Astrophys.* (ed. F. Martins, S. Boissier, V. Buat, L. Cambrésy & P. Petit), pp. 419–422.

Radko, T. 2003 A mechanism for layer formation in a double-diffusive fluid. *J. Fluid Mech.* **497**, 365–380.

Radko, T. 2010 Equilibration of weakly nonlinear salt fingers. *J. Fluid Mech.* **645**, 121–143.

Radko, T. 2013 *Double-Diffusive Convection*. Cambridge University Press.

Rincon, F. 2019 Dynamo theories. *J. Plasma Phys.* **85**, 205850401.

Romeo, N., Słomka, J., Dunkel, J. & Burns, K.J. 2024 Vortex line entanglement in active Beltrami flows. *J. Fluid Mech.* **982**, A12.

Shah, K., Chini, G. P., Caulfield, C. P. & Garaud, P. 2024 Regimes of stratified turbulence at low Prandtl number. *J. Fluid Mech.* **998**, A60.

Skoutnev, V.A. & Beloborodov, A.M. 2024 Zones of Tayler instability in stars , arXiv: 2411.08492.

Słomka, J. & Dunkel, J. 2017 Spontaneous mirror-symmetry breaking induces inverse energy cascade in 3D active fluids. *Proc. Natl. Acad. Sci.* **114**, 2119–2124.

Tobias, S.M. 2021 The turbulent dynamo. *J. Fluid Mech.* **912**, P1.

Traxler, A., Stellmach, S., Garaud, P., Radko, T. & Brummell, N. 2011 Dynamics of fingering convection. Part 1 Small-scale fluxes and large-scale instabilities. *J. Fluid Mech.* **677**, 530–553.

Wang, D. & Ruuth, S.J. 2008 Variable step-size implicit-explicit linear multistep methods for time-dependant partial differential equations. *J. Comp. Math.* **26**, 838–855.

Xie, J.-H., Miquel, B., Julien, K. & Knobloch, E. 2017 A reduced model for salt-finger convection in the small diffusivity ratio limit. *Fluids* **2** (1), 6.